



Power Electronic Systems  
Laboratory

© 2017 JSME

JSME Mechanical Engineering Journal, June 2017

## Experimental Verification of an Angle-Sensorless Control Scheme for Bearingless Permanent Magnet Machines

T. Wellerdieck,  
T. Nussbaumer,  
J. W. Kolar

This material is published in order to provide access to research results of the Power Electronic Systems Laboratory / D-ITET / ETH Zurich. Internal or personal use of this material is permitted. However, permission to reprint/republish this material for advertising or promotional purposes or for creating new collective works for resale or redistribution must be obtained from the copyright holder. By choosing to view this document, you agree to all provisions of the copyright laws protecting it.



Eidgenössische Technische Hochschule Zürich  
Swiss Federal Institute of Technology Zurich

**Advance Publication by J-STAGE**

**Mechanical Engineering Journal**

DOI:10.1299/mej.17-00003

Received date : 31 December, 2016

Accepted date : 13 June, 2017

J-STAGE Advance Publication date : 21 June, 2017

# Experimental verification of an angle-sensorless control scheme for bearingless permanent magnet machines

Tobias WELLERDIECK\*, Thomas NUSSBAUMER\*\* and Johann W. KOLAR\*

\* Power Electronic Systems Laboratory, ETH Zurich

Physikstrasse 3, 8092, Zurich, Switzerland

E-mail: [wellerdieck@lem.ee.ethz.ch](mailto:wellerdieck@lem.ee.ethz.ch)

\*\* Levitronix GmbH

Technoparkstrasse 1, 8005, Zurich, Switzerland

## Abstract

Bearingless machines are used for a variety of applications with demand for low mechanical loss, low wear and low contamination. These machines use contact-free magnetic suspension to levitate the rotor. The control of the machine requires precise radial and angular position information in order to ensure stable levitation. This information is usually obtained with two types of sensors: radial displacement sensors and angle sensors. Alternatively, an angle-sensorless control scheme can be used, reducing the complexity and the cost of the machine. While such a control is well known for conventional machines it is challenging to adapt it for bearingless machines. The reason is that most methods fail to provide the angle information at zero and at low speed but bearingless machines require knowledge about the rotor angle at all speeds in order to function. The theoretical mode of operation of a model based angle observer for zero and low speed operation of a bearingless machine was shown in previous publications. The observer obtains the rotor angle estimation error by analyzing the performance of the radial bearing and comparing it to the performance of a model with zero angle error. This observer can be used for operation at standstill and over the whole speed range. This paper provides a more detailed description of the non-idealities of the zero and low speed observer and presents results of machine operation without angle sensors. The generation of torque and force inside the machine is analyzed in more detail. Furthermore, it is shown how to combine the novel observer with a conventional, back electromotive force based, high speed angle observer. The experimentally verified results of this paper indicate that the novel observer can be used up to speeds at which back electromotive force estimation is possible. This allows the efficient, angle-sensorless operation of the machine over the whole speed range.

**Key words** : Bearingless machine, Angle observer, Model based, Sensorless, Low speed, Zero speed

## 1. Introduction

Bearingless machines are electric motors that combine the functions of an electric machine and a magnetic bearing in one stator, (Bichsel 1991), allowing for a compact machine design. The motor generates both the torque and the suspension forces required to levitate the rotor. This allows the elimination of a drive shaft and mechanical bearings and enables the rotor to be driven inside a sealed compartment, making bearingless machines well suited for applications with demands on high speed (Mitterhofer, Gruber, and Amrhein 2014), low wear and low particle generation (Neff, Barletta, and Schoeb 2002).

The rotor of the machine described in this paper consists of a ring shaped one pole-pair, radially-magnetized rare-earth magnet with a diameter that exceeds its height. This type of machine is called a heteropolar bearingless permanent magnet slice motor (Schoeb and Barletta 1995). The disk shape is chosen because it simplifies the control of the machine. Only the radial position and the rotor angle have to be actively controlled while axial movement and tilting around the radial axis are stable by design (Schoeb and Barletta 1997; Amemiya et al. 2005). Figure 1(b) depicts a

render of the bearingless machine, showing the ring shape of the magnet, the stator iron and the windings that are used to produce the magnetic fields in the airgap. Parts of the mechanical structure and the case are not shown to make the ring shaped rotor and the stator structure visible.

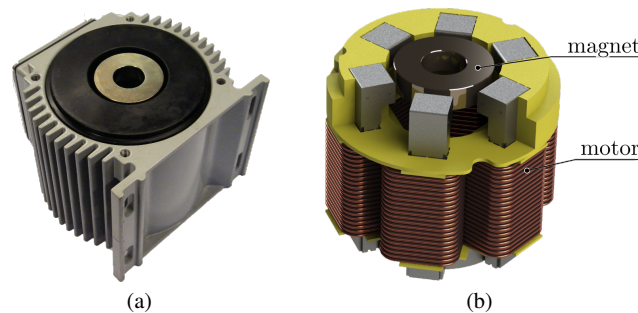


Fig. 1 The bearingless machine that is used to verify the control scheme (a) and a render of the machine showing the ring shaped rotor (b). Note that the rotor magnet is radially displaced in order to generate the displacement force required for the angle estimation.

The controller of the bearingless machine requires knowledge of both the radial and the angular rotor position in order to ensure stable levitation and high drive performance (Nussbaumer et al. 2011). The position is commonly obtained with the use of radial and angular sensor systems that are usually complex and sensitive to harsh environments. Omitting these sensors reduces the complexity and the cost. This can make bearingless machines suitable for applications in rough environments or applications with high cost sensitivity.

This paper focuses on the possibility to eliminate the angular position sensors. Multiple angle-sensorless rotor angle estimation techniques for permanent magnet synchronous machines have been reported in the literature (J.-S. Kim and Sul 1997; Acarnley and Watson 2006). These methods are of two types: the first type is based on the estimation of the back-electromotive force (EMF) (Park et al. 2001) and the second type uses high frequency (HF) signal injection (S. Kim and Ha 2008). The EMF based control schemes work only above a minimum speed since they require sufficient amplitude of the induced voltage, which is proportional to the machine speed. Therefore, these methods are not suitable for zero- and low-speed operation. The HF signal injection methods rely on the fact that the machine inductances are dependent on the rotor angle due to saliency of the machine. While the latter method provides rotor angle information over the entire speed range of the machine it is limited to machines with salient pole rotors. Furthermore, the machine inductances in bearingless machines are also dependent on the radial rotor position. Therefore, a deviation in the radial position of the rotor will disturb the rotor angle estimation.

It is possible to use EMF based observers in combination with a special low speed control method and drive the machine with a two stage controller. This approach is reported in literature by Raggl et al. (2009). The control scheme utilizes an open loop controller for zero and low speed operation. The term low speed operation is used in this paper for the speed range at which the EMF based observer cannot be employed. This paper proposes to replace the open-loop control with a closed-loop zero and low speed angle estimator. The zero and low speed angle estimator is model based, meaning that it utilizes a model of the bearing and compares the ideal model behavior with the actual bearing behavior. The novel observer allows to drive the machine up to the minimum speed at which EMF based methods can take over. This paper presents a control scheme consisting of the novel, model based, zero and low speed angle observer and a conventional, EMF based, high speed observer.

The derivations of the model based observer presented in this paper are based on two assumptions: a non-zero mean rotor angle estimation error is acceptable and no magnetic saturation in the iron circuit of the machine occurs. The former assumption limits the applicability of the control scheme to bearingless machines with magnetic bearings that are reasonably robust against angle errors. The latter assumption is usually met during operation with a small drive torque and, therefore, a small drive current. Possible areas of application for the control scheme presented in this paper are bearingless motors used in pumps and blowers since the load torque and the drive current of such machines depend quadratically on the rotational speed. Magnetic saturation of the iron circuit does not occur during low torque operation at small speeds since the iron circuit is optimized for the magnetic flux at the rated drive current. Furthermore, the additional bearing losses due to the non-zero mean rotor angle estimation error at low speeds are tolerable since the torque and speed dependent drive losses are small. Note that the magnetic saturation in the iron circuit is only problematic for the model

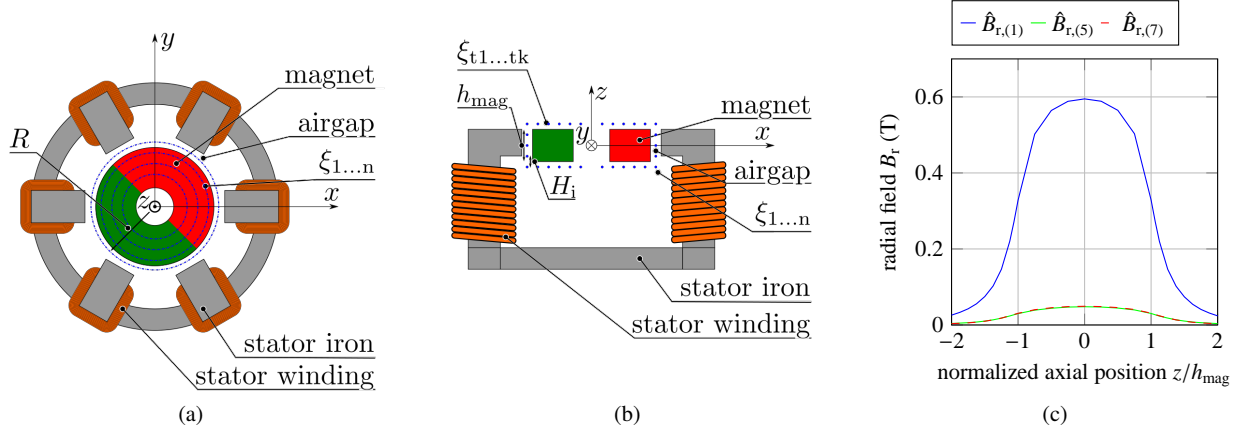


Fig. 2 Schematic top view (a) and side view (b) of the bearingless motor. The flux density is analyzed on the circles  $\xi_{1\dots n}$  on a cylindrical surface around and two disks above and below the rotor. The amplitude of the radial component of the most prominent flux density harmonics in the airgap over axial position (c) showing that the flux is not constrained to the rotor height.

based zero and low speed observer. The high speed, EMF based observer can be used when magnetic saturation is present. The evaluation of different areas of application or the adaption of the control scheme for machines that exhibit magnetic saturation in the iron circuit at low speed and/or torque lies outside the scope of this paper.

The modelling of the magnetic flux around the rotor is shown in Section 2. The results of the flux modelling are used for the analysis of the torque and bearing force generation in the bearingless machine, which is presented in Section 3. Section 4 presents the functionality and the structure of the angle-sensorless control scheme. The initial angle detection, the model based zero and low speed angle observer and the high speed observer are described in detail. The functionality of the observer is shown in Section 5 by measurements taken with the prototype machine shown in Fig. 1(a). Section 6 draws some conclusions, summarizes the results and gives some outlook on how the control scheme can be improved further.

## 2. Modelling of magnetic flux around the rotor magnet

The torque and bearing force calculation is based on the analysis of the magnetic flux density in the airgap, similar to the analysis presented by Laptre et al. (2015). A FEM program was used to obtain the magnetic flux density around the rotor. Figure 2(a) and Fig. 2(b) show a schematic top and side view of the motor. The flux density analysis is done on the circles  $\xi_{1\dots n}$  on a cylindrical surface in the airgap and on disks above and below the rotor. Note that the number of circles is reduced in the figures for the sake of clarity, the simulation is done for  $n = 43$ . This number offers a good trade-off between precision and computational time for the given geometry. The analysis of the flux density above and below the rotor is necessary since the short rotor has significant stray fields. The stray fields become larger if the rotor is displaced. The consideration of the stray fields is the most significant difference to the reduced analysis presented by Wellerdieck, Nussbaumer, and Kolar (2016).

The flux density  $B$  around the rotor can be approximated by its space harmonics  $B_{k(i)}$  as

$$B_k(\alpha) \approx \sum_i \hat{B}_{k(i)} \cos(i\alpha + \phi_{k(i)}), k \in [(r, t, z), (x, y, z)] \quad (1)$$

with  $\hat{B}_{k(i)}$ ,  $\phi_{k(i)}$  and  $\alpha$  being the amplitude of the  $i$ -th harmonic, the phase of the harmonic and the angular position on one of the circles  $\xi$ , respectively. Equation (1) is used with cylindrical coordinates in the airgap and with cartesian coordinates on the top and bottom disks. Figure 2(c) shows the amplitude of the radial component of the fundamental, the fifth and seventh flux density harmonic for different axial positions in the airgap. The fifth and the seventh harmonic are dominant for a non-displaced rotor due to the geometry of the stator. This shows that the magnetic flux is not limited to the height of the rotor and an extension of the analysis to the top and bottom of the rotor is necessary.

The magnetic fields around the rotor are dependent on the rotor position as well as the bearing and drive currents in the stator windings. If magnetic saturation is neglected, the amplitudes of the flux density harmonics can be calculated as a sum of four field components as

$$\hat{B}_{k(i)} = \hat{B}_{k(i),0}(\theta) + \hat{B}_{k(i),\Delta}(\theta, \Delta x, \Delta y) + \hat{B}_{k(i),D}(\hat{I}_D, \phi_D) + \hat{B}_{k(i),B}(\hat{I}_B, \phi_B), k \in [(r, t, z), (x, y, z)] \quad (2)$$

Table 1 The variables that define the magnetic flux density around the rotor.

variable	description	range
$\Delta x$	displacement in $x$ direction	$\Delta x \in [-2 \text{ mm}, 2 \text{ mm}]$
$\Delta y$	displacement in $y$ direction	$\Delta y \in [-2 \text{ mm}, 2 \text{ mm}]$
$\theta$	rotor angle	$\theta \in [0, 2\pi]$
$\hat{I}_D, \phi_D$	drive current amplitude and phase	$\hat{I}_D \in [0, 10 \text{ A}], \phi_D \in [0, 2\pi]$
$\hat{I}_B, \phi_B$	bearing current amplitude and phase	$\hat{I}_B \in [0, 3 \text{ A}], \phi_B \in [0, 2\pi]$

and the phases can be stated as

$$\phi_{k,(i)} = \phi_{k,(i),0}(\theta) + \phi_{k,(i),\Delta}(\theta, \Delta x, \Delta y) + \phi_{k,(i),D}(\phi_D) + \phi_{k,(i),B}(\phi_B), k \in [(r, t, z), (x, y, z)]. \quad (3)$$

Table 1 lists the variables used in (2) and (3). A protective cup is placed in the airgap limiting the maximum displacement of the rotor to

$$\sqrt{(\Delta x)^2 + (\Delta y)^2} = 2 \text{ mm}. \quad (4)$$

The drive and bearing currents during nominal operation are limited to  $\hat{I}_D = 15 \text{ A}$  and  $\hat{I}_B = 5 \text{ A}$  to prevent magnetic saturation of the iron circuit. Table. 2 shows how the relevant harmonics can be assigned to different field components in the airgap.

Table 2 The four field components and their relevant harmonics.

description	amplitude and phase	relevant harmonic number
zero displacement field	$\hat{B}_{k,(i),0}, \phi_{k,(i),0}$	$i \in [1, 5, 7, 11, 13]$
rotor displacement field	$\hat{B}_{k,(i),\Delta}, \phi_{k,(i),\Delta}$	$i \in [1 - 10]$
drive field	$\hat{B}_{k,(i),D}, \phi_{k,(i),D}$	$i \in [1, 5, 7, 11, 13]$
bearing field	$\hat{B}_{k,(i),B}, \phi_{k,(i),B}$	$i \in [2, 4, 8, 10, 12, 14, 16]$

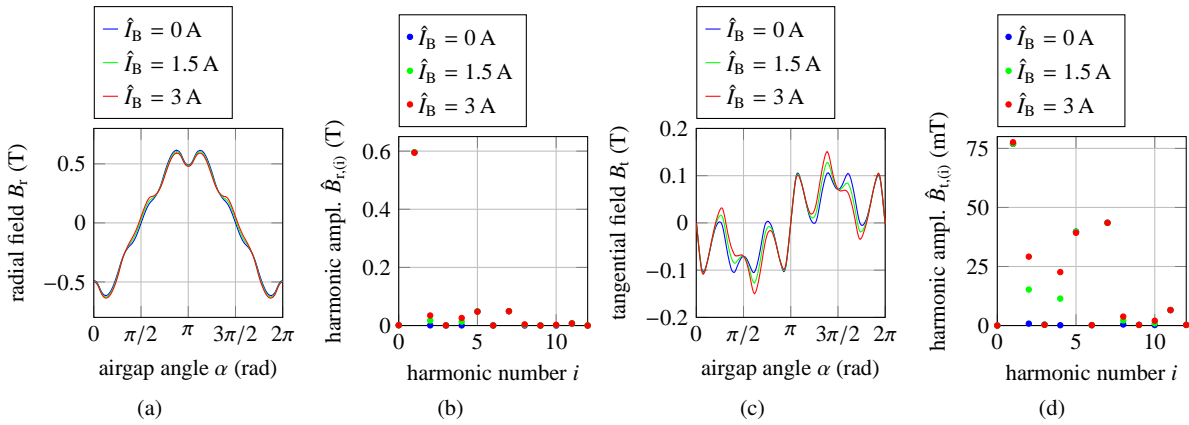


Fig. 3 The field in the middle of the airgap at  $z = 0 \text{ mm}$  for an undisplaced rotor and different bearing current amplitudes, with the radial field (a), the amplitudes of the radial space harmonics (b), the tangential field (c) and the amplitudes of the tangential space harmonics (d). Only a limited number of space harmonics are dependent on the bearing current.

The concept of the relevant harmonics can be explained best by an example. Figure 3(a) and 3(c) show the radial and tangential field on the circle  $\xi_{22}$  with the axial position  $z = 0$ , cf. Fig. 2(b). The middle position is chosen because the  $z$  component of the field is negligible due to symmetry. The bearing current is varied from 0 A to 3 A, while the rotor is at  $\Delta x = \Delta y = 0 \text{ mm}$ . Figure 3(b) and 3(d) show the amplitudes of the space harmonics  $\hat{B}_{r,(i)}$  and  $\hat{B}_{t,(i)}$ . The constant amplitudes of the harmonics of the order 1, 5 and 7 of the zero displacement field are clearly visible. It can be seen that only the harmonics of the order 2, 4, 8, 10 and 12 change with increasing bearing current while the other harmonics stay constant. The change of the amplitude is linear.

Only a small number of FEM simulations with different bearing current amplitudes are required to formulate a good model for the bearing field in the airgap. The same analysis can be done for the displacement and the drive field in the airgap and for the fields above and below the rotor. The advantage of this approach is that the field model, once it is formulated with the use of FEM simulations, can be evaluated computationally efficient. The model could even be implemented on the digital signal processor (DSP) of the controller to predict the bearing forces precisely.

### 3. Drive and bearing behavior

The torque and force acting on the rotor magnet can be calculated by evaluating the Maxwell stress tensor on a closed surface around the rotor. In this section, only magnetostatic forces are considered. The cylindrical surface is split into 43 parts and the magnetic flux density on each part of the surface is approximated by the most relevant space harmonics, cf. Section 2. Therefore, the surface integration becomes an integration on  $n = 43$  cylinder parts on the circles  $\xi_{1,\dots,n}$ , cf. Fig. 2(a) and Fig.2(b). The cylinder parts around the rotor can be divided into three domains. There are  $k$  cylinder parts above the rotor,  $l - k$  parts in the airgap and  $n - l$  parts below the rotor. The cylinder parts in the domain above,  $\xi_{1,\dots,k}$ , and below the rotor,  $\xi_{l,\dots,n}$ , are used to account for stray fields around the rotor. The torque due to the field in the airgap can be calculated as

$$\begin{aligned}
 T_{z,c,ag} &= \frac{R^2}{\mu_0} \sum_i^n H_i \int_0^{2\pi} B_{r,ci}(\alpha) B_{t,ci}(\alpha) d\alpha \\
 F_{x,c,ag} &= \frac{R}{2\mu_0} \sum_i^n H_i \int_0^{2\pi} \left\{ (B_{r,ci}^2(\alpha) - B_{t,ci}^2(\alpha) - B_{z,ci}^2(\alpha)) \cos(\alpha) - 2B_{r,ci}(\alpha) B_{t,ci}(\alpha) \sin(\alpha) \right\} d\alpha \\
 F_{y,c,ag} &= \frac{R}{2\mu_0} \sum_i^n H_i \int_0^{2\pi} \left\{ (B_{r,ci}^2(\alpha) - B_{t,ci}^2(\alpha) - B_{z,ci}^2(\alpha)) \sin(\alpha) + 2B_{r,ci}(\alpha) B_{t,ci}(\alpha) \cos(\alpha) \right\} d\alpha \\
 F_{z,c,ag} &= \frac{R}{\mu_0} \sum_i^n H_i \int_0^{2\pi} B_{r,ci}(\alpha) B_{z,ci}(\alpha) d\alpha
 \end{aligned} \tag{5}$$

with  $T_{z,c,ag}$  being the torque in  $z$  direction and  $F_{x,c,ag}, F_{y,c,ag}, F_{z,c,ag}$  being the forces acting on the rotor. The radius of the circles in the airgap,  $\xi_{k+1,\dots,l-1}$ , is denoted by  $R$  and the height of the  $i$ -th cylinder part is labeled  $H_i$ . The flux density components on the  $i$ -th cylinder part in radial, tangential and  $z$ -direction are labeled  $B_{r,ci}, B_{t,ci}$  and  $B_{z,ci}$ , respectively. The forces acting on the rotor due to the stray fields below and above the rotor can be calculated in a similar manner, resulting in the torque  $T_{c,z,stray}$  and the forces  $F_{x,c,stray}, F_{y,c,stray}, F_{z,c,stray}$ . The total force acting on the rotor is

$$\begin{aligned}
 T_{z,c} &= T_{z,c,ag} + T_{z,c,stray} \\
 F_{x,c} &= F_{x,c,ag} + F_{x,c,stray} \\
 F_{y,c} &= F_{y,c,ag} + F_{y,c,stray} \\
 F_{z,c} &= F_{z,c,ag} + F_{z,c,stray}.
 \end{aligned} \tag{6}$$

The formulation of the force and torque calculation due to the stray fields as well as the specification of the predominant stray field harmonics are omitted for the sake of clarity.

Equation (5) in combination with the reduced harmonics approach allows for the precise calculation of the torque and bearing forces acting on the rotor. The calculation is computationally efficient since only additions and multiplications are required. However, the calculations become extensive if all the harmonics of Tab. 2 are used. Therefore, an example with a reduced number of harmonics is used to illustrate the behavior of the machine. The simplifications are: the  $z$  component of the field is neglected, the zero displacement field consists only of harmonics of the order 1 while the bearing and the displacement field consist only of harmonics of the order 2. It is assumed that the rotor is levitating at the position  $x = x^* > 0, y = y^* = 0$  and  $\theta = \hat{\theta} = 0$ , with  $x, y$  denoting the rotor position,  $x^*, y^*$  denoting the reference rotor position and  $\theta, \hat{\theta}$  denoting the rotor angle and the estimated rotor angle, respectively. Figure 4(a) shows a schematic view of this mode of operation with  $\vec{\Psi}_r, \vec{F}_\Delta$  and  $\vec{F}_B$  denoting the flux direction of the permanent magnet, the force acting on the magnet due to the displacement and the bearing force, respectively. The field in the airgap is

$$\begin{aligned}
 B_{r,(1)}(\alpha) &= \hat{B}_{r,(1),0} \cos(\alpha) \\
 B_{t,(1)}(\alpha) &= \hat{B}_{r,(1),0} \cos(\alpha - \pi/2) \\
 B_{r,(2)}(\alpha) &= \hat{B}_{r,(2),\Delta} \cos(2\alpha) + \hat{B}_{r,(2),B} \cos(2\alpha + \pi) \\
 B_{t,(2)}(\alpha) &= \hat{B}_{r,(2),\Delta} \cos(2\alpha - \pi/2) + \hat{B}_{r,(2),B} \cos(2\alpha + \pi/2).
 \end{aligned} \tag{7}$$

The field components are listed in Tab. 2. The amplitudes and harmonics fulfill

$$\begin{aligned}
 \hat{B}_{r,(2),B} &= \hat{B}_{r,(2),\Delta} & \hat{B}_{t,(2),B} &= \hat{B}_{t,(2),\Delta} \\
 \phi_{r,(2),B} &= \phi_{r,(2),\Delta} + \pi & \phi_{t,(2),B} &= \phi_{t,(2),\Delta} + \pi.
 \end{aligned} \tag{8}$$

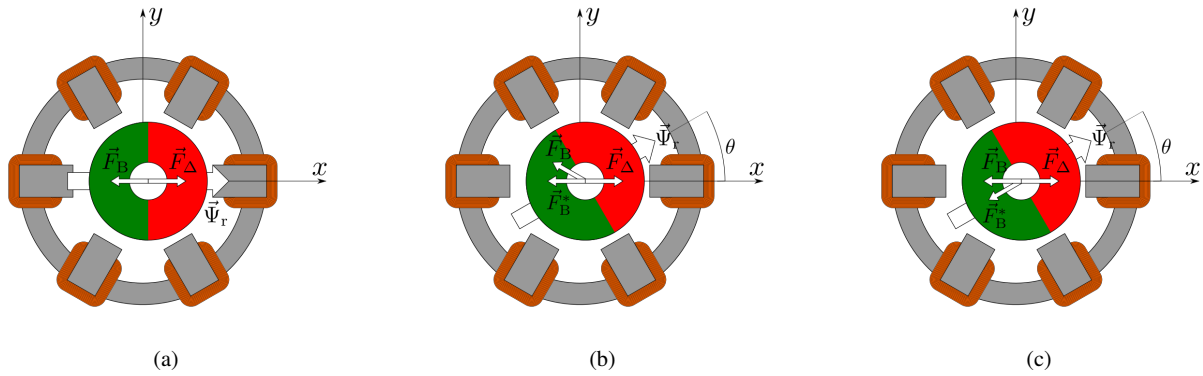


Fig. 4 Schematic top view of the bearingless machine showing an operating point with zero rotor angle estimation error (a), operating point with non-zero angle estimation error without (b) and with (c) the compensation of the bearing controllers.

The bearing controller of the machine has set the bearing current such that the net force acting on the rotor is

$$\vec{F} = \begin{bmatrix} F_x \\ F_y \end{bmatrix} = \vec{F}_\Delta - \vec{F}_B = 0. \quad (9)$$

This is done by measuring the displacement  $x, y$ , calculating the bearing current  $\vec{I}_B = \begin{bmatrix} I_{Bx} \\ I_{By} \end{bmatrix}$  in the rotor coordinate system and then rotating the bearing current by  $\hat{\theta}$  into the stator coordinate system.

The above is the normal, stable behavior of a bearing controller with correct rotor information. Now, it is assumed that the rotor angle  $\theta$  is changed to  $\theta > 0$  while the rotor angle estimation is kept at  $\hat{\theta} = 0$ , cf. Fig. 4(b) and Section 4.2. The bearing controller still applies the same bearing current since neither the radial position nor the angle estimation have changed. The resulting flux density in the airgap is

$$\begin{aligned} B_{r,(1)}(\alpha) &= \hat{B}_{r,(1),0} \cos(\alpha - \theta) \\ B_{t,(1)}(\alpha) &= \hat{B}_{r,(1),0} \cos(\alpha - \theta - \pi/2) \\ B_{r,(2)}(\alpha) &= \hat{B}_{r,(2),\Delta} \cos(2\alpha - \theta) + \hat{B}_{r,(2),B} \cos(2\alpha + \pi) \\ B_{t,(2)}(\alpha) &= \hat{B}_{r,(2),\Delta} \cos(2\alpha - \theta - \pi/2) + \hat{B}_{r,(2),B} \cos(2\alpha + \pi/2). \end{aligned} \quad (10)$$

Inserting (10) into (5) results a non-zero net force acting on the rotor. The reason is that the reference bearing force  $\vec{F}_B^*$  is not the same as the actual bearing force  $\vec{F}_B$ . The rotor will move in  $y$  direction because the bearing current is not rotated by the correct rotor angle. The bearing force acting on the rotor can be expressed in terms of  $\vec{F}_B^*$  and the angle estimation error  $\Delta\theta = \hat{\theta} - \theta$  as

$$\vec{F}_B = \begin{bmatrix} \cos(\Delta\theta) & -\sin(\Delta\theta) \\ \sin(\Delta\theta) & \cos(\Delta\theta) \end{bmatrix} \vec{F}_B^*. \quad (11)$$

The movement in  $y$  direction will be detected by the  $y$ -direction position controller. The  $y$ -axis bearing controller will adjust for this movement and reduce  $I_{By}$ . Figure 4(c) shows the effect of this. The reference bearing force has been rotated by the two bearing controllers until  $\vec{F}_B = \vec{F}_\Delta$  is fulfilled and the rotor is moved to its reference position.

Equation (11) describes an approximation of the actual coupling. It is correct for the simple example with only first and second order harmonics. Figure 5(a) shows the forces acting on a displaced rotor with the rotor angle being changed from 0 to  $2\pi$  while the estimated angle is kept  $\hat{\theta} = 0$ . The forces calculated with all the harmonics shown in Tab. 2 are labeled  $F_{x,c}, F_{y,c}$  and the forces calculated with the simplified approach are denoted  $F_{x,s}, F_{y,s}$ . This shows that (11) really is only a rough estimation. However, Section 5 shows that the estimation is sufficiently precise to control the machine.

In this section it has been shown how an error in the rotor position results in a coupling of the bearing control in  $x$  and  $y$  direction. This coupling effect is used to calculate the rotor angle estimation error and to update the rotor angle estimate. The method works only for small estimation errors since the radial position controllers fail to stabilize the rotor if the coupling is too strong.

## 4. Observer structure

### 4.1. Initial angle detection

The initial angle estimation is possible if the rotor is not levitating by evaluating the radial position sensors as shown by Raggl et al. (2009). The method is based on the fact that the rotor always lands on a rotor pole. Therefore, the direction of magnetization  $\hat{\theta}_{\text{mag}}$  can be estimated by

$$\hat{\theta}_{\text{mag}} = \arctan\left(\frac{\Delta y_0}{\Delta x_0}\right), \quad (12)$$

with  $\Delta y_0$  and  $\Delta x_0$  being the radial initial positions of the machine. However, it is not clear which pole is touching the wall. Therefore, the initial angle estimate  $\hat{\theta}_{\text{init}}$  can be

$$\hat{\theta}_{\text{init}} = \hat{\theta}_{\text{mag}}, \text{ or} \quad (13)$$

$$\hat{\theta}_{\text{init}} = \hat{\theta}_{\text{mag}} + \pi \quad (14)$$

In a first step it is assumed that (13) holds. The rotor reference position is set to  $x^* = y^* = 0$ . The radial position controllers will set the reference radial force  $\vec{F}_{\text{B}}^*$  to

$$\vec{F}_{\text{B}}^* = \vec{r}_0 - \vec{r}^* = \begin{bmatrix} x_0 \\ y_0 \end{bmatrix} - \begin{bmatrix} x^* \\ y^* \end{bmatrix}. \quad (15)$$

If the assumption is correct, the bearing force  $\vec{F}_{\text{B}}$  is aligned to  $\vec{F}_{\text{B}}^*$  and the rotor is lifted off the wall. However, if (13) does not hold true,

$$\angle(\vec{F}_{\text{B}}) - \angle(\vec{F}_{\text{B}}^*) = \pi, \quad (16)$$

must be true, according to (11). Therefore, the bearing force acts in the direction of the displacement and the rotor will not move radially. If this is the case,  $\hat{\theta}_{\text{init}}$  is set according to (14) and the rotor is brought to levitation. A small drive current is applied to generate a one-pole pair stator field in the direction of the magnetization during start-up. This stator field, and the cogging torque clamp the rotor, ensuring a constant rotor angle.

The drive currents are analyzed once the rotor has reached the rotor reference position  $x^* = y^* = 0$  in order to determine if the gravitational force is pulling in radial or in axial direction. A gravitational force in radial direction will lead to a non-zero mean bearing current in opposite direction of the gravitational force. It is assumed that the gravitational pull does not change during operation since it is only dependent on the orientation of the machine. The control scheme switches to the model based angle observer once the rotor has reached the reference position and the gravitational pull is known.

### 4.2. Zero and low speed observer

The angle observer utilizes the force coupling described in (11) to estimate the rotor angle estimation error and the fact that the two bearing controllers will compensate the coupling for small angle estimation errors.

Figure 5(b) shows a schematic controller block diagram of the bearingless machine. The speed control is not shown and the sensors are modelled to work without measurement error. Furthermore, the current controllers are assumed to work perfectly and, therefore, are not shown. Note, that  $s$  is the Laplace operator and  $m$  is the rotor mass. The two radial position controllers are labeled  $C_x(s)$  and  $C_y(s)$  and are of a PID structure. The bearing controllers calculate the bearing current reference in the rotor oriented coordinate system  $I_{\text{Bx}}^*$  and  $I_{\text{By}}^*$  based on the difference between the rotor position

$$r = \begin{bmatrix} x \\ y \end{bmatrix} \quad (17)$$

and the rotor reference position

$$r^* = \begin{bmatrix} x^* \\ y^* \end{bmatrix}. \quad (18)$$

The bearing currents are then rotated into the stator coordinate system in the block  $T$ .  $B(s)$  denotes the force generation in the machine. Double integration of the sum of the internal forces  $F_x$  and  $F_y$  and any external radial forces acting on

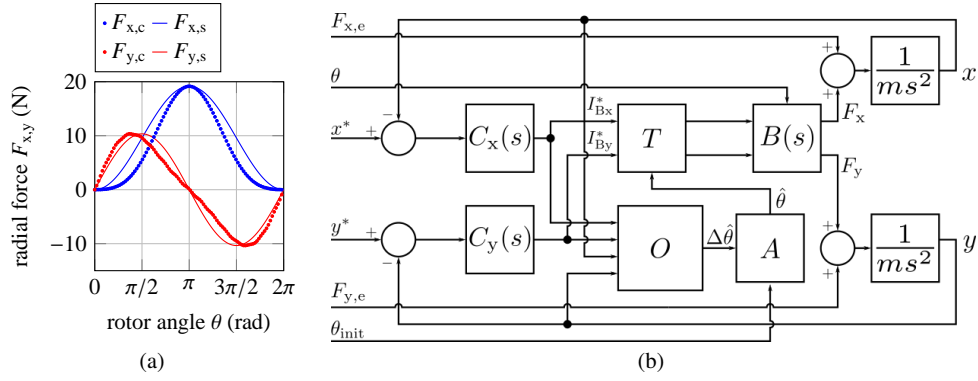


Fig. 5 Radial forces acting on a displaced rotor if the rotor is rotated but the rotor angle estimate is not updated (a) and simplified controller block diagram of the bearingless machine neglecting the current controllers and the speed control (b).

the rotor  $F_{x,e}$  and  $F_{y,e}$  yields the rotor position. The rotor angle estimation observer is labeled  $O$  and the angle estimation update function is labeled  $A$ .

The observer block  $O$  calculates an estimate of the rotor angle error as

$$\Delta\hat{\theta} = \angle(\vec{F}_B^*) - \angle(\hat{\vec{F}}_{r,e}) - \pi = \angle(\vec{I}_B) - \angle(\hat{\vec{F}}_{r,e}) - \pi. \quad (19)$$

The bearing current angle is known since the bearing currents are defined by the radial position controllers. The estimated external radial force  $\hat{\vec{F}}_{r,e}$  is a part of the radial external force  $\vec{F}_{r,e}$  and consists of:

$$\hat{\vec{F}}_{r,e} = \vec{F}_\Delta + \vec{F}_g = \vec{F}_{r,e} - \vec{F}_\delta \quad (20)$$

with  $\vec{F}_\Delta$ ,  $\vec{F}_g$  and  $\vec{F}_\delta$  being the force due to radial displacement of the rotor, the radial gravitational pull and any disturbance forces, respectively. The angle of the displacement force is

$$\angle(\vec{F}_\Delta) = \angle(\vec{r}) \quad (21)$$

with  $\vec{r}$  being the radial displacement. Therefore, the angle of the displacement force can be calculated based on the measurements of the radial rotor position  $x, y$ . The rotor is displaced if no radial gravitational pull is detected in order to generate a known  $\hat{\vec{F}}_{r,e}$ .

The observer presented in this paper provides an estimation of the angle error. Subsequently, the angle estimation is calculated in the update function  $A$  by updating the angle estimation with

$$\hat{\theta}(t) = \hat{\theta}_{init} + P \cdot \Delta\theta(t) + I \cdot \int_0^t \Delta\theta(\tau) d\tau \quad (22)$$

with  $P, I$  being the proportional and integrator gain. The integrator part is required to drive the estimated error to zero.

The unknown disturbance forces  $\vec{F}_\delta$  are usually application dependent or arise from rotor imbalances. However, application dependent disturbances are usually speed dependent, such as hydraulic forces in fans or pumps, and so are imbalance forces. Nevertheless, any disturbance force will lead to an undetectable angle estimation error  $\Delta\hat{\theta}_\delta$ . The biggest undetectable estimation error  $\Delta\hat{\theta}_\delta$  occurs if the disturbance force is perpendicular to the known radial forces and can be calculated as

$$\Delta\hat{\theta}_\delta = \arctan\left(\frac{|\vec{F}_\delta|}{|\vec{F}_\Delta + \vec{F}_g|}\right). \quad (23)$$

### 4.3. High speed angle observer

The high speed observer is based on the estimation on the EMF. The EMF based observer is able to estimate the rotor angle with sufficient precision for machine speeds exceeding 10 % of the maximum machine speed. This limit is dependent on the machine, as well as the accuracy and the bandwidth of the drive current and terminal voltage measurements in the power electronic system driving the machine.

The EMF voltage and, subsequently the stator flux  $\vec{\Psi}_S$  and the rotor flux  $\vec{\Psi}_R$ , can be derived from measurements of the terminal voltages  $\vec{U}_D$  and the drive currents  $\vec{I}_D$  by

$$\vec{\Psi}_S = \int (\vec{U}_D - R_S \vec{I}_D) dt$$

$$\vec{\Psi}_R = \vec{\Psi}_S - L_S \vec{I}_D \quad (24)$$

with the resistance of the machine winding  $R_S$  and the stator inductance  $L_S$ , (Wellerdieck, Peralta, et al. 2015). The rotor angle estimate is calculated by

$$\theta = \angle(\vec{\Psi}_R). \quad (25)$$

The high speed observer is switched on as soon as the machine speed exceeds 10 % of the maximal machine speed. First, it is used in parallel to the low and zero speed observer. The angle used for controlling the machine is a speed dependent weighted average of the two estimation methods. Only the high speed observer is used for machine speeds exceeding 15 % of the maximum speed. The zero and low speed angle observer is then switched off and the rotor reference position is then set to  $x^* = y^* = 0$  in order to minimize bearing current losses.

## 5. Verification

The verification is done with the bearingless machine shown in Fig. 1(a). The control of the machine is executed on a digital signal processor (DSP). The DSP communicates with a computer and allows to display register values directly. The machine was placed with the gravity pulling in radial direction of the rotor. The rotor is displayed in the direction of the gravitational pull for use with the zero- and low speed observer in order to minimize the undetectable observation error according to (23).

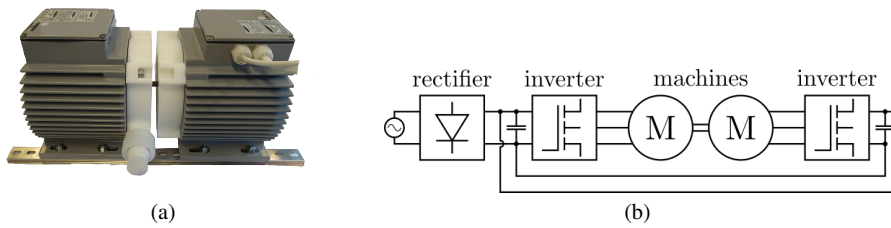


Fig. 6 Set-up with two machines with mechanically connected rotors used for load tests (a) and schematic depiction showing the connection of the power electronics (b).

The machine is operated both in a no-load operation and with controlled braking torque. Figure 6(a) shows the torque test set-up. The rotors of two identical machines are mechanically coupled and the machines are placed coaxially. The DC links of the two driving inverters are connected to balance the power and only one rectifier is used, cf. Fig. 6(b). The machines are operated with braking torques up to 50 % of the nominal torque during low speed operation. The torque is limited since the machines use a combined winding scheme, such that the sum of bearing and drive current during operation with displaced rotor must not exceed the rated current of the machine. The rotor of the braking machine is also displaced if the driving machine uses the novel zero and low speed observer in order to prevent a tilting of the two rotors.

Both machines are equipped with angle sensors to measure the rotor angle  $\theta_m$ . The braking machine is operated solely with the sensors. The driving machine is controlled with the angle-sensorless control scheme and the sensors are used to measure the angle estimation error  $\Delta\theta = \hat{\theta} - \theta_m$ .

The external radial force  $\vec{F}_{r,e}$  is generated by setting the rotor reference position to  $x^* = 0.5 \text{ mm}$ ,  $y^* = 0.5 \text{ mm}$  during operation with the low and zero speed observer. This constitutes to approximately 50 % of the mechanical air gap of the machine.

Figure 7(a) shows the operation of the machine without load, meaning that the braking machine is not connected. The machine speed is 500 rpm. Figures 7(b), 7(c), 7(d) and 7(e) show operation of the machine with the zero and low speed observer and a load torque of 50 % of the maximum torque at 500 rpm, 1000 rpm, 1500 rpm and 2000 rpm, respectively. The zero and low speed observer is able to estimate the rotor angle with sufficient precision to ensure stable levitation. The angle estimation error  $\Delta\theta_m$  is non-zero mostly due to the torque component that arises from the displacement and due to the simplified coupling matrix outlined in (11). The estimation error also leads to a varying machine speed since the speed estimate is derived from the estimated angle. Figure 7(f) shows the angle obtained by the high speed observer at 2000 rpm at 50 % of nominal torque. Note that the results show the estimated angle and the estimation error for multiple rotations.

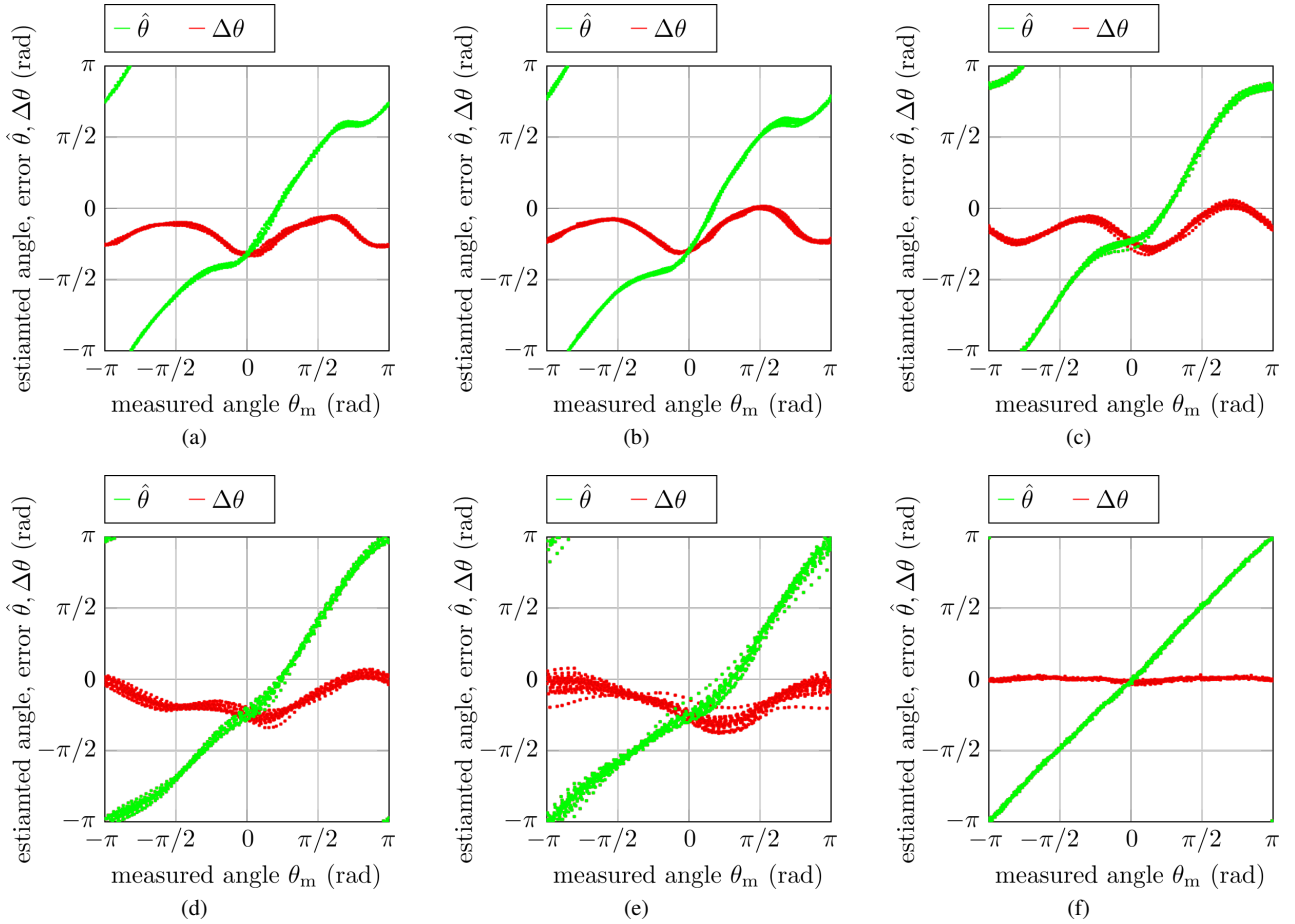


Fig. 7 Mean estimated angle and angle estimation error of the zero- and low speed observer for multiple rotations over measured rotor angle for no load operation at 500 rpm (a) and for 50 % of nominal torque at 500 rpm (b), at 1000 rpm (c), at 1500 rpm (d) and at 2000 rpm (e). Mean estimated angle and angle estimation error for the high speed observer over measured rotor angle for 50 % of nominal torque at 2000 rpm (f).

The machine was also tested with the zero and low speed model based observer for higher speeds for the sake of completeness. Figure 8(a) and Fig. 8(b) show the angle estimation and the error for a machine speed of 50 % and 70 % of the nominal speed for the no load condition. The mean angle estimation error  $\overline{\Delta\theta}$  over  $K$  revolutions is

$$\overline{\Delta\theta} = \frac{1}{2K\pi} \int_0^{2K\pi} \Delta\theta dt. \quad (26)$$

The results illustrated in Figs. 7(a) to 7(e) show a mean angle estimation error  $\overline{\Delta\theta} < 0$ , which corresponds to an estimated angle  $\hat{\theta}$  that is lagging the rotor angle  $\theta$ . The mean angle estimation error can be reduced by increasing the integral gain  $I$  of the observer function (22). However, this leads to a reduced dynamic of the observer which limits the steepness of a rotor angle ramp that can be tracked, i.e. limits the acceleration of the rotor. This represents a trade-off between mean steady state angle estimation error and maximum rotor acceleration. The results shown in Figs. 7(a) to 7(e) were obtained with the low speed observer which was tuned to achieve the highest possible acceleration while ensuring an acceptable mean angle estimation error. The behavior of an observer which is not optimized for high dynamics but for a small mean steady state error is shown in Fig. 8(c) and Fig. 8(d) for a machine speed of 250 rpm and 500 rpm, respectively. The mean angle estimation error can be significantly reduced if low dynamics are acceptable.

The verification shows that the angle observer is able to estimate the rotor angle with sufficient accuracy both at low and at high machine speeds. It is clearly possible to accelerate the machine to the required speed to switch to an EMF based estimation. The verification also shows that a conventional, EMF based observer outperforms the zero and low speed observer with respect to estimation accuracy at speeds where it is applicable. A comparison of the estimation accuracy of the EMF based observer and the model based observer at low speeds is shown in Fig. 8(c) and Fig. 8(d) for a machine speed of 250 rpm and 500 rpm, respectively. The machine control utilizes the estimated angle of the model based observer to drive the machine, the estimated angle of the EMF based observer is recorded for comparison. Low-

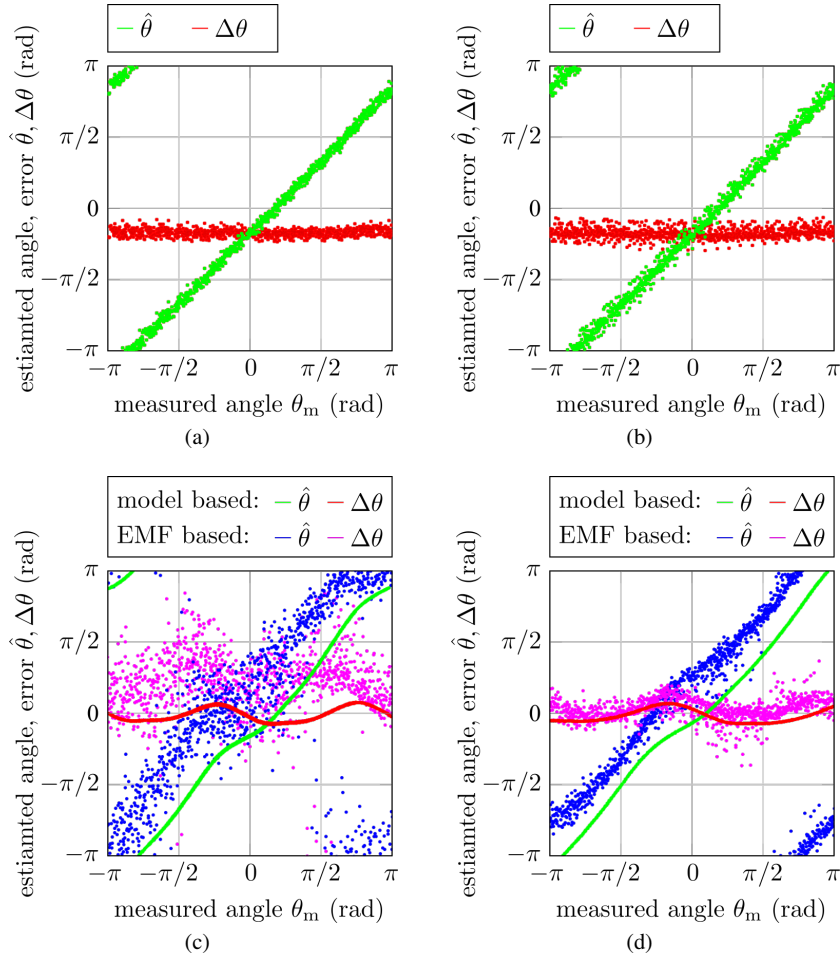


Fig. 8 Mean estimated angle and angle estimation error of the zero and low speed observer for multiple rotations over measured rotor angle for no load operation at 5000 rpm (a) and at 7000 rpm (b). Comparison of the performance of the EMF based and the model based observer at 250 rpm (c) and at 500 rpm (d). Note that both observers are tuned such that the controller dynamics are comparable, resulting in small steady state errors for the model based observer.

pass filtering of the drive currents, which are utilized to obtain the flux estimation, c.f. (24), results in an acceptable estimation quality at 500 rpm. The low-pass filtering of the currents reduces the achievable dynamic of the bearingless machine. Therefore, the comparison is carried out with a model based observer with equally low dynamics. The signal to noise ratio of the current sensors is very low at 250 rpm due to the speed dependent magnitude of the EMF-voltage. The angle estimation obtained with the EMF based observer becomes noisy. Achieving stable levitation with such an angle estimation is difficult.

## 6. Conclusion

The angle observer structure shown in this paper allows for the detection of the rotor angle at zero- and low machine speeds in bearingless machines. The observer is based on the fact that a rotor angle estimation error leads to a coupling of the radial position control in  $x$  and  $y$  direction. This coupling can be measured by evaluating the bearing currents. The observer uses an initial rotor angle estimation and updates it continuously. The method is based on the assumption that the radial disturbance forces acting on the rotor are small. The validity of this assumption is depending on the application of the bearingless machine and the maximum speed at which the observer is used.

The functionality of the method is shown by measurements with a prototype. The model based observer is able to provide an angle estimation at low speed, where no back-EMF based observer can be used, and up to the nominal machine speed. This allows the model based observer to be used as a back-up angle estimation method for any EMF based observer.

The quality of the angle estimation can be improved if the coupling matrix, cf. (11), is adapted to represent the effect

of all the harmonics. This would then allow to also adapt the angle estimation function shown in (19).

## Acknowledgement

This work was supported by the *Swiss Commission for Technology and Innovation CTI-KTI*.

## References

- Acarney, P.P. and Watson, J.F. "Review of position-sensorless operation of brushless permanent-magnet machines". In: *Industrial Electronics, IEEE Transactions on* 53.2 (Apr. 2006), pp. 352–362.
- Amemiya, J., Chiba, A., Dorrell, D.G., and Fukao, T. "Basic characteristics of a consequent-pole-type bearingless motor". In: *Magnetics, IEEE Transactions on* 41.1 (Jan. 2005), pp. 82–89.
- Bichsel, J. "The Bearingless Electrical Machine". In: *Proc. 1th Int. Symp. Magnetic Suspension Technology* (June 1991), pp. 561–573.
- Kim, Joohn-Sheok and Sul, Seung-Ki. "New approach for high-performance PMSM drives without rotational position sensors". In: *Power Electronics, IEEE Transactions on* 12.5 (Sept. 1997), pp. 904–911.
- Kim, Sung-Yeol and Ha, In-Joong. "A New Observer Design Method for HF Signal Injection Sensorless Control of IPMSMs". In: *Industrial Electronics, IEEE Transactions on* 55.6 (June 2008), pp. 2525–2529.
- Lapre, B., Takorabet, N., Meibody-Tabar, F., Fontchastagner, J., Lateb, R., and Silva, J. D. "New Model of Radial Force Determination in Bearingless Motor". In: *IEEE Transactions on Magnetics* 51.3 (Mar. 2015), pp. 1–4.
- Mitterhofer, H., Gruber, W., and Amrhein, W. "On the High Speed Capacity of Bearingless Drives". In: *IEEE Transactions on Industrial Electronics* 61.6 (June 2014), pp. 3119–3126.
- Neff, M., Barletta, N., and Schoeb, R. "Bearingless centrifugal pump for highly pure chemicals". In: *Proc. 5th Int. Symp. Magnetic Bearings* (2002), pp. 283–287.
- Nussbaumer, T., Karutz, P., Zurcher, F., and Kolar, J.W. "Magnetically Levitated Slice Motors - An Overview". In: *Industry Applications, IEEE Transactions on* 47.2 (Mar. 2011), pp. 754–766.
- Park, Han-Woong, Lee, Sang-Hoon, Won, Tae-Hyun, Kim, Moon-Soo, and Kim, Cheul-U. "Position sensorless speed control scheme for permanent magnet synchronous motor drives". In: *Proc. on ISIE International Symposium on Industrial Electronics* 1 (2001), 632–636 vol.1.
- Raggl, K., Warberger, B., Nussbaumer, T., Burger, S., and Kolar, J.W. "Robust Angle-Sensorless Control of a PMSM Bearingless Pump". In: *Industrial Electronics, IEEE Transactions on* 56.6 (June 2009), pp. 2076–2085.
- Schoeb, R. and Barletta, N. "Magnetic Bearing. Principle and Application of a Bearingless Slice Motor." In: *JSME International Journal Series C Mechanical Systems, Machine Elements and Manufacturing* 40.4 (1997), pp. 593–598.
- Schoeb, R. and Barletta, N. "Principle and Application of a Bearingless Slice Motor". In: *Proc. 5th Int. Symp. Magnetic Bearings* (May 1995), pp. 313–318.
- Wellerdieck, T., Nussbaumer, T., and Kolar, J. "Angle-Sensorless Zero- and Low-Speed Control of Bearingless Machines". In: *IEEE Transactions on Magnetics* PP.99 (2016), pp. 1–1.
- Wellerdieck, T., Peralta, P., Nussbaumer, T., and Kolar, J. W. "Contributions to an ultra-high temperature (250 C/500 F) bearingless pump". In: *Proc. of the 18th International Conference on Electrical Machines and Systems (ICEMS)* (Oct. 2015), pp. 1158–1164.